



Response of drought to climate extremes in a semi-arid inland river basin in China

QU Zhicheng, YAO Shunyu, LIU Dongwei*

School of Ecology and Environment, Inner Mongolia University, Hohhot 010021, China

Abstract: Against the backdrop of global warming, climate extremes and drought events have become more severe, especially in arid and semi-arid areas. This study forecasted the characteristics of climate extremes in the Xilin River Basin (a semi-arid inland river basin) of China for the period of 2021–2100 by employing a multi-model ensemble approach based on three climate Shared Socioeconomic Pathway (SSP) scenarios (SSP1-2.6, SSP2-4.5, and SSP5-8.5) from the latest Coupled Model Intercomparison Project Phase 6 (CMIP6). Furthermore, a linear regression, a wavelet analysis, and the correlation analysis were conducted to explore the response of climate extremes to the Standardized Precipitation Evapotranspiration Index (SPEI) and Streamflow Drought Index (SDI), as well as their respective trends during the historical period from 1970 to 2020 and during the future period from 2021 to 2070. The results indicated that extreme high temperatures and extreme precipitation will further intensify under the higher forcing scenarios (SSP5-8.5>SSP2-4.5>SSP1-2.6) in the future. The SPEI trends under the SSP1-2.6, SSP2-4.5, and SSP5-8.5 scenarios were estimated as $-0.003/a$, $-0.004/a$, and $-0.008/a$, respectively, indicating a drier future climate. During the historical period (1970–2020), the SPEI and SDI trends were $-0.003/a$ and $-0.016/a$, respectively, with significant cycles of 15 and 22 a, and abrupt changes occurring in 1995 and 1996, respectively. The next abrupt change in the SPEI was projected to occur in the 2040s. The SPEI had a significant positive correlation with both summer days (SU) and heavy precipitation days (R10mm), while the SDI was only significantly positively correlated with R10mm. Additionally, the SPEI and SDI exhibited a strong and consistent positive correlation at a cycle of 4–6 a, indicating a robust interdependence between the two indices. These findings have important implications for policy makers, enabling them to improve water resource management of inland river basins in arid and semi-arid areas under future climate uncertainty.

Keywords: climate extremes; climate change; Standardized Precipitation Evapotranspiration Index (SPEI); Streamflow Drought Index (SDI); wavelet analysis; multi-model ensemble; Xilin River Basin

Citation: QU Zhicheng, YAO Shunyu, LIU Dongwei. 2024. Response of drought to climate extremes in a semi-arid inland river basin in China. *Journal of Arid Land*, 16(11): 1505–1521. <https://doi.org/10.1007/s40333-024-0064-5>; <https://cstr.cn/32276.14.JAL.02400645>

1 Introduction

It is widely acknowledged that current global warming is caused by the massive emission of greenhouse gases during the era of rapid industrialization (Su et al., 2015). Li et al. (2023) predicted that the increase in global average temperature will reach or even exceed 1.5°C above the pre-industrial level over the next two decades. Furthermore, multiple regions around the world will face unprecedented climate change impacts, including an increase in climate extremes and drought events.

*Corresponding author: LIU Dongwei (E-mail: liudw@imu.edu.cn)

Received 2024-05-11; revised 2024-09-03; accepted 2024-09-16

© The Author(s) 2024

The impact of global warming on the water cycle is significantly manifested by the acceleration of evaporation and precipitation processes (Wang et al., 2024b). As temperatures rise, the atmosphere shows an increased capacity for holding water vapor, which not only accelerates the rate of evaporation but also alters the patterns and intensities of precipitation (Samuel et al., 2023). Influenced by global warming, this enhanced evaporation, intensified precipitation, and further impacted river flows and lake levels, thus altering the spatiotemporal distribution of water resources. If global temperatures rise by 1.5°C–4.0°C above the pre-industrial level, the probability of compound drought-flood events will significantly increase worldwide (Rezvani et al., 2023). Moreover, the severe damage caused by climate extremes raises significant concerns for human health, social development, and ecological stability (Savage et al., 2021). Climate change has the potential to worsen climate extremes, including intense precipitation and prolonged high temperatures. The combination of rising temperatures and erratic precipitation patterns significantly increases the risk of natural disasters. Furthermore, drought conditions in arid and semi-arid areas are likely to worsen due to the increased potential evaporation resulting from global warming (Chikabvumbwa et al., 2024). For example, São Paulo of Brazil faced a severe drought in 2014, reducing the city's water supply capacity to 15% of normal levels, affecting approximately 1.10×10^7 people (Ballarin et al., 2021). In the summer of 2018, Northeast China endured a 33-d heatwave, resulting in 3000 fatalities (Ren et al., 2020). Even the Arctic Circle has recently recorded an unprecedented temperature of 38.0°C, leading to wildfires that engulfed a land area of 0.79×10^4 km². Over 41% of the Earth's surface is arid and semi-arid land; these areas contain more than 40% of the world's population, and also have a rich biodiversity (Tripathi et al., 2024). However, in arid and semi-arid areas, the limited water resources and fragile ecosystems amplify the risks to environmental resources posed by climate change. It is imperative for various industries, such as water management, agriculture, and manufacturing, to understand the past changes in climate extremes and anticipate their future trends. Consequently, the changes in climate extremes and drought events triggered by global warming have received significant attention worldwide.

Runoff is a crucial component of water supply and plays a key role in maintaining the security and diversity of regional ecosystems (Zhao et al., 2022). However, the response of runoff to climate change is complex and uncertain, posing significant challenges to regional water resource management. Although the total volume of water in the hydrological cycle remains constant, the growing gap between the limited availability of freshwater and the increasing population is becoming more pronounced. In arid and semi-arid areas, many streams are prone to drying up, leading to a marked decrease in water resource availability in river basins (Zhang et al., 2020b). The adverse effects of precipitation and temperature extremes on runoff resources have intensified. Consequently, understanding the variations in climate extremes and hydrological events in water-scarce areas is vital for ensuring water security. From this prospective, access to reliable and robust information regarding future changes in climate-related extremes is critical for public adaptation to climate change.

Previous studies have primarily focused on the connection between climate extremes and meteorological drought (Su et al., 2021; Zhao et al., 2023; Mohammed et al., 2024), while the impacts of these factors on surface hydrological drought have been overlooked. With recent advances in modeling techniques, the coupling relationship between hydrology and climate has become a research hotspot. Thus, this study comprehensively investigated the relationships and evolving patterns among climate extremes, meteorological drought, and hydrological drought. The Xilin River Basin, located in the semi-arid area of the Mongolian Plateau, is an inland river basin in China. Characterized by a temperate continental climate, the river basin possesses a fragile natural environment and is extremely sensitive to climate change. In recent years, the increasing frequency of climate extremes has exacerbated the drought issues in the region, with flow interruptions becoming more frequent. Thus, this study analyzed the patterns of climate extremes and drought events in the Xilin River Basin from 1970 to 2020, projected the evolution of climate extremes and meteorological drought under various scenarios over the next 50 a and

investigated the interconnection between climate extremes and drought phenomena, to provide scientific guidance on mitigating climate extreme hazards and managing water resources in inland river basins of semi-arid areas.

2 Materials and methods

2.1 Study area

The Xilin River Basin ($43^{\circ}26'–44^{\circ}39'N$, $115^{\circ}05'–117^{\circ}17'E$) is located in the central part of the Xilin Gol League, Inner Mongolia Autonomous Region, China. The basin covers an area of 1.08×10^4 km² and has an average elevation of 989 m (Fig. 1). It is located within the semi-arid continental climatic area with an average annual temperature of $1.7^{\circ}C$. The Xilin River, which exhibits distinct inland semi-arid climatic features, primarily relies on precipitation for replenishment, resulting in rapid response of water level to precipitation changes. The basin receives an average annual precipitation of 266.8 mm, which is unevenly distributed throughout the year, with more than half of the total annual precipitation occurring in the summer months (Zhou et al., 2024).

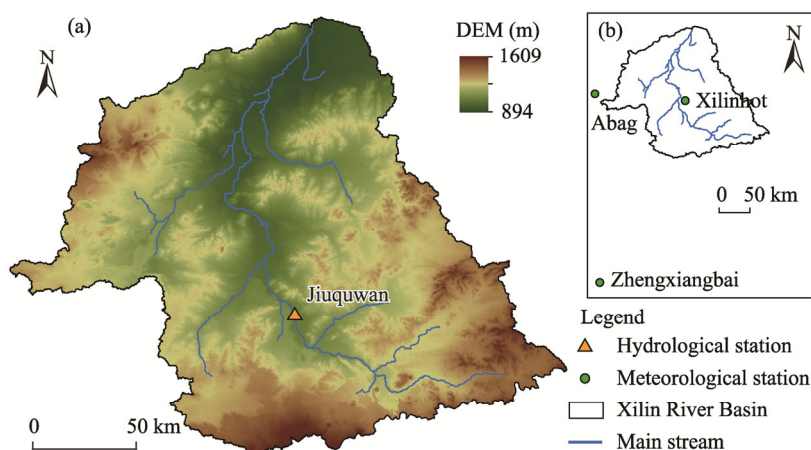


Fig. 1 Overview of the Xilin River Basin based on the digital elevation model (DEM) and the location of hydrological station (a), as well as the spatial distribution of meteorological stations (b)

2.2 Data collection

Daily maximum temperature, daily minimum temperature, and daily precipitation data during the historical period from 1970 to 2020 were obtained from three meteorological stations in the Xilin River Basin (Fig. 1). Daily runoff data for the Xilin River was provided by the Jiuquwan hydrological station. Future precipitation and temperature projections during the period of 2021–2070 were obtained from the Scenario Model Intercomparison Project (Scenario MIP) of the latest Coupled Model Intercomparison Project Phase 6 (CMIP6). In Scenario MIP, Global Climate Models (GCMs) are informed by Shared Socioeconomic Pathways (SSPs), reflecting development trajectories under various climate and socio-economic scenarios. This study employed SSP1-2.6 (an idealized sustainable development pathway), SSP2-4.5 (a continuation of the current development model), and SSP5-8.5 (a scenario emphasizing increased reliance on fossil fuels) to represent low, medium, and high forcing scenarios for future climate projections, respectively. The GCMs provide detailed insights into climate change predictions, including projections of climate extremes. Several studies have used GCM outputs from the Coupled Model Intercomparison Project Phase 5 (CMIP5) to analyze and simulate future climate trends and their extremes (Villarini and Vecchi, 2012; Harrison et al., 2015; Yu et al., 2021). Zhu et al. (2021)

found that CMIP6 is superior to the CMIP5, particularly in simulating extreme precipitation, due to the incorporation of more comprehensive and complex factors. To enhance the precision of climate model outputs, we selected five widely recognized GCM outputs for global climate change studies, as shown in Table 1.

Table 1 Details of the CMIP6 GCMs used in the study

Sequence number	Model name	Country	Institution	Resolution
1	BCC-CSM2-MR	China	Beijing Climate Center, China Meteorological Administration	320×160
2	IPSL-CM6A-LR	France	Institute Pierre Simon Laplace	144×143
3	MIROC6	Japan	Model for Interdisciplinary Research on Climate	256×128
4	MPI-ESM1-2-HR	Germany	Max Planck Institute for Meteorology	384×192
5	MRI-ESM2-0	Japan	Meteorological Research Institute	320×160

Note: CMIP6, Coupled Model Intercomparison Project Phase 6; GCMs, Global Climate Models.

2.3 Methods

2.3.1 Data processing

The climate scenarios in CMIP6 are based on the Representative Concentration Pathways (RCPs) of the earlier stages, which integrate different SSPs to represent future social and economic development (Zhang et al., 2019b). However, GCMs still have limitations in the study of medium- and small-scale regions because the spatial resolution is usually only 1°, even in the CMIP6. Preprocessing the data is necessary due to the inevitable coarse spatial resolution and systematic biases of GCMs. Therefore, we processed the GCM data sequentially for downscaling, multi-aggregate modeling, and bias correction. Taylor diagrams were used to depict the effects after a data bias correction. The components in the diagram included the correlation coefficient, the standard deviation, and the root mean square error. In the Taylor diagrams, each data point represents data processed by different methods. Generally, the data point closest to the observation point is considered the simulation result that most closely approximates the true value, and is therefore used for analysis in the study. Statistical downscaling methods are frequently used to downscale the prediction data from GCMs. These methods are widely recognized as one of the most useful approaches for handling climate data (Liu et al., 2023). Multi-model ensembles can effectively integrate the advantages of a single climate model to reduce the stochastic errors of the model. Furthermore, to diminish the uncertainty of the predicted data, we applied the reliability ensemble averaging (REA) method for bias correction of the CMIP6 multi-model ensemble (Sun et al., 2016). The REA method primarily considers the model convergence index (reflecting the consistency of model simulation results) and the model performance index (indicating the model's efficacy in simulating climate) for model weighting. Additionally, a bias factor and a distance factor were applied to assign weights to each model, prioritizing those models with a higher simulation accuracy. The weighting criteria used in the REA method were established by Gao et al. (2008). Using temperature as an example, the equation is expressed as follows:

$$W_i = \left[(R_{B,i})^m \times (R_{D,i})^n \right]^{\left[\frac{1}{m \times n} \right]} \alpha = \left[\left(\frac{\varepsilon_T}{|B_{T,i}|} \right)^m \times \left(\frac{\varepsilon_T}{|D_{T,i}|} \right)^n \right]^{\left[\frac{1}{m \times n} \right]}, \quad (1)$$

and the weighted ensemble average for each meteorological station was calculated as follows:

$$\Delta T_{\text{mean}} = \frac{\sum_i W_i \Delta T_i}{\sum_i W_i}, \quad (2)$$

where W_i is the weight assigned to the i^{th} model; $R_{B,i}$ represents the inverse of the absolute bias for the i^{th} model, where B stands for bias and i refers to the i^{th} model in the ensemble; m is the influence coefficient for the model bias; $R_{D,i}$ is the absolute distance between the model output and the weighted ensemble average, where D stands for the distance; n is the influence coefficient for model consistency; α is the natural variability adjustment factor; $B_{T,i}$ refers to the absolute bias of the i^{th} model for temperature ($^{\circ}\text{C}$), where T stands for the temperature ($^{\circ}\text{C}$); ε_T is a measure of natural variability, ensuring that the model outputs with a small bias would not be unjustly handled; $D_{T,i}$ is the distance between the model output and the weighted ensemble average, and is calculated by an iterative procedure; ΔT_{mean} is the REA average output of temperature ($^{\circ}\text{C}$); and ΔT_i is the change in temperature output by the separate model ($^{\circ}\text{C}$). ΔT_{mean} and ΔT_i were then used to recalculate the distance of separate models as $D_{T,i} = \Delta T_i - \Delta T_{\text{mean}}$. The process was iterated continuously through the above steps until convergence was reached, thereby obtaining both the weights and final results.

2.3.2 Climate extremes

In this study, six representative climate extreme indices defined by the Expert Team on Climate Change Detection and Indices (ETCCDI) (Medeiros et al., 2022) were selected: frost days (FD), summer days (SU), Max Tmax (TXx; monthly maximum value of daily maximum temperature), number of heavy precipitation days (R10mm), consecutive wet days (CWD), and consecutive dry days (CDD), as shown in Table 2. Here, FD, SU, and TXx are extreme temperature indices, and R10mm, CWD, and CDD are extreme precipitation indices. These indices covered the historical period of 1970–2020 and future period of 2021–2070 under the three SSP-RCP scenarios (SSP1-2.6, SSP2-4.5, and SSP5-8.5). These six indices were chosen because they represent the commonly used and dominant climate extremes. Moreover, they have been extensively employed in previous studies of climate variability across different regions (Sun et al., 2016; Almazroui, 2019).

Table 2 Definitions of the six climate extremes used in this study

Identification	Indicator name	Definition	Unit
FD	Frost days	Annual count when daily minimum temperature (TN) $< 0.0^{\circ}\text{C}$	d
SU	Summer days	Annual count when daily maximum temperature (TX) $> 25.0^{\circ}\text{C}$	d
TXx	Max Tmax	Monthly maximum value of daily maximum temperature	$^{\circ}\text{C}$
R10mm	Heavy precipitation days	Annual count of days when precipitation ≥ 10.0 mm	d
CWD	Consecutive wet days	Maximum number of consecutive days with daily precipitation ≥ 1.0 mm	d
CDD	Consecutive dry days	Maximum number of consecutive days with daily precipitation < 1.0 mm	d

2.3.3 Drought indices

Although precipitation is a primary index of drought conditions, Omer et al. (2020) reported that the impact of potential evapotranspiration is significant, particularly in the context of global warming. The Standardized Precipitation Evapotranspiration Index (SPEI) is considered to be more appropriate for climate change studies than the Standardized Precipitation Index (SPI), and it has been widely used in previous research (Dong et al., 2023; Gumus, 2023). This preference for the SPEI arises from its incorporation of potential evapotranspiration in the drought index calculation. The SPEI is derived from the water balance equation, which calculates the daily difference between precipitation and potential evapotranspiration. In this study, due to data limitations, potential evapotranspiration was estimated using the temperature-based Thornthwaite method (Thornthwaite, 1948). The SPEI was obtained by normalizing the difference between precipitation and potential evapotranspiration in this study. The general procedure for calculating the SPEI is as follows:

First, the difference between precipitation and potential evapotranspiration was calculated:

$$S_z = \text{PRE}_z - \text{PET}_z, \quad (3)$$

where S_z is the climatic water balance over a period of z months (mm); PRE_z is the precipitation in the z months (mm); and PET_z is the potential evapotranspiration in the z months (mm).

Second, a three-parameter log-logistic probability distribution function was applied to normalize and fit the sequence of the cumulative value of the difference between precipitation and potential evapotranspiration over a timescale, with the cumulative probability function ($f(x)$) and cumulative probability density function ($F(x)$) described as follows:

$$f(x) = \frac{\beta}{\theta} \left(\frac{x - \gamma}{\theta} \right)^{\beta-1} \left[1 + \left(\frac{x - \gamma}{\theta} \right)^{\beta} \right]^{-2}, \quad (4)$$

$$F(x) = \left[1 + \left(\frac{\theta}{x - \gamma} \right)^{\beta} \right]^{-1}, \quad (5)$$

where θ , β , and γ are the scale parameter, shape parameter, and origin parameter, respectively. These parameters can be obtained from a linear matrix.

Third, standardizing the cumulative probability density function was accomplished to obtain the SPEI using the following formula:

$$\text{SPEI} = w - \frac{C_0 - C_1 w + C_2 w^2}{1 + d_1 w + d_2 w^2 + d_3 w^3}; \quad w = \sqrt{-2 \ln(P)}, \quad (6)$$

where w is an intermediate variable derived from the natural logarithm of P (where P is the probability of exceedance of S), transforming the probability into a value associated with the standard normal distribution. The constants C_0 , C_1 , C_2 , d_1 , d_2 , and d_3 are specific to the standard normal distribution and have the values of 2.515517, 0.802853, 0.010328, 1.432788, 0.189269, and 0.001308, respectively. In this study, the SPEI at a 12-month timescale was calculated using the 'SPEI' package in the R software (<https://www.r-project.org/>). The Streamflow Drought Index (SDI) uses the Gamma (Γ) distribution probability to characterize the runoff variations. It normalizes runoff data, particularly those with a skewed probability distribution, and categorizes drought levels based on the standardized cumulative frequency distribution of runoff. The SDI was calculated as follows:

$$\text{SDI} = \phi^{-1} \left(\frac{u - 0.44}{v + 0.12} \right), \quad (7)$$

where ϕ is the standard normal distribution; u is the ascending order ranking of hydroclimatic variables; and v is the number of observed or simulated data points. Laimighofer and Laaha (2022) showed that drought indices spanning a 12-month timescale can more accurately capture the evolution of drought conditions than indices calculated over shorter periods. Consequently, the SPEI and SDI at the 12-month timescale were used here to effectively analyze the long-term characteristics of drought variations in the Xilin River Basin. The classification of drought is shown in Table 3.

Table 3 Drought severity classification based on the SPEI and SDI

Grade	SPEI	SDI	Drought level
1	$-1.0 < \text{SPEI} \leq -0.5$	$-1.0 < \text{SDI} \leq -0.5$	Mild drought
2	$-1.5 < \text{SPEI} \leq -1.0$	$-1.5 < \text{SDI} \leq -1.0$	Moderate drought
3	$-2.0 < \text{SPEI} \leq -1.5$	$-2.0 < \text{SDI} \leq -1.5$	Severe drought
4	$\text{SPEI} \leq -2.0$	$\text{SDI} \leq -2.0$	Extreme drought

Note: SPEI, Standardized Precipitation Evapotranspiration Index; SDI, Streamflow Drought Index.

2.3.4 Wavelet analysis

Common wavelet analysis methods include the Morlet wavelet, wavelet coherence, and Dmey wavelet (Sang, 2013). The Morlet wavelet, which is characterized as a complex-form wavelet, has distinct advantages over real-form wavelets when analyzing trend changes (Bilgili et al., 2022). This superiority stems from the $\pi/2$ phase shift between its real and imaginary parts, which eliminates oscillation in the coefficient modes during the wavelet transformation of real-form wavelets. Consequently, this prevents the separation of the mode and bit phase components from their wavelet coefficients. The Morlet wavelet can also be used to analyze the intrinsic patterns of complex time series data at different time scales (Kuskaya, 2022). Given these benefits, the Morlet wavelet was used in this study to conduct continuous wavelet transform analyses on the time series data of climate extremes, and the SPEI and SDI values. The wavelet coherence was used to describe the consistency of variations between two series at different time scales, as characterized by their amplitude and phase information (Fattah et al., 2024). The wavelet coherence not only reveals the correlation and significance between two variables at different time scales, but also has considerable analytical advantages in low-energy regions (Nourani et al., 2021). Therefore, the wavelet coherence was used in this study to capture the local correlations between runoff and climate extremes in the time and frequency domains. The Morlet wavelet and wavelet coherence are widely used in the study of climate change and runoff patterns (Nayak et al., 2013; Gao et al., 2024).

3 Results

3.1 Data calibration

Before analyzing the GCM data, we used the observed data as a reference to verify the accuracy of the model outputs (Fig. 2). Figure 2 shows that by applying the statistical downscaling processes and REA method, the GCM outputs were brought into closer alignment with observations. There were differences in the simulation effects of the different climate models, with the five GCMs simulating the highest temperatures better than the lowest temperatures. Additionally, the simulation performance was significantly better for temperature than for precipitation. For all factors, the correlation coefficient between the REA model averaging result and the observed data was higher than the result from the single model.

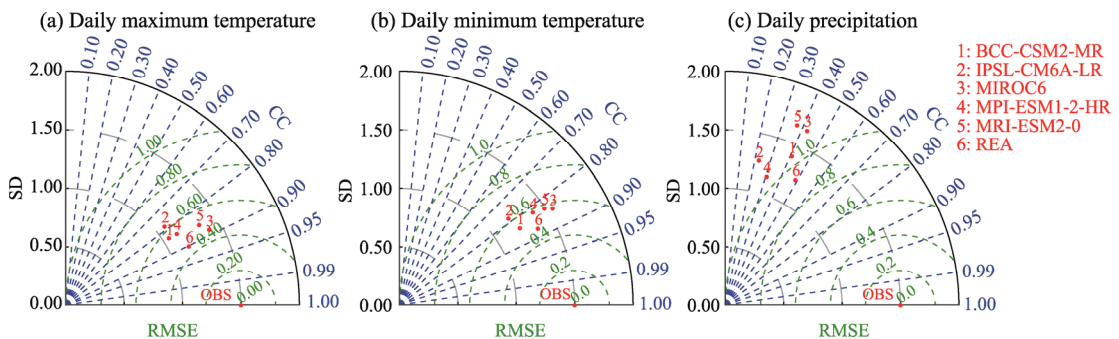


Fig. 2 Taylor diagrams comparing the daily maximum temperature (a), daily minimum temperature (b), and daily precipitation (c) from five Global Climate Models (GCMs) and reliability ensemble averaging (REA) results with observation (OBS) in the Xilin River Basin during the period of 1970–2020. SD, standard deviation; CC, correlation coefficient; RMSE, root mean square error.

3.2 Characteristics of climate extremes

3.2.1 Prediction of climate extremes

Figure 3 shows the evolution of climate extreme indices in the Xilin River Basin. The overall trends in climate extremes under the three future scenarios were consistent, with the intensity

diminishing in the order of SSP5-8.5, SSP2-4.5, and SSP1-2.6. During the period of 1970–2020, four indices (SU, TXx, R10mm, and CWD) exhibited positive trends, while two indices (FD and CDD) exhibited negative trends. Both FD and SU reflect the frequency of extreme temperature events. Under the three climate scenarios (SSP1-2.6, SSP2-4.5, and SSP5-8.5), the frequency of extreme low-temperature events (FD) decreased at rates of 17, 23, and 29 d/100 a, respectively, with a progressively intensifying rate of decline. This decrease was more pronounced than the increase in SU, except for the SSP5-8.5 scenario. For TXx, which measures the intensity of extreme temperatures, there were increases of 3.2°C/100 a, 3.3°C/100 a, and 4.8°C/100 a, respectively, under the three climate scenarios (SSP1-2.6, SSP2-4.5, and SSP5-8.5). As indices of the frequency and duration of extreme precipitation events, R10mm and CWD respectively exhibited an upward trend under the future scenarios, albeit with relatively small changes (within a range of 1–4 d/100 a). Conversely, CDD, indicating the duration of dry spells, exhibited a significant decreasing trend under the three climate scenarios (SSP1-2.6, SSP2-4.5, and SSP5-8.5).

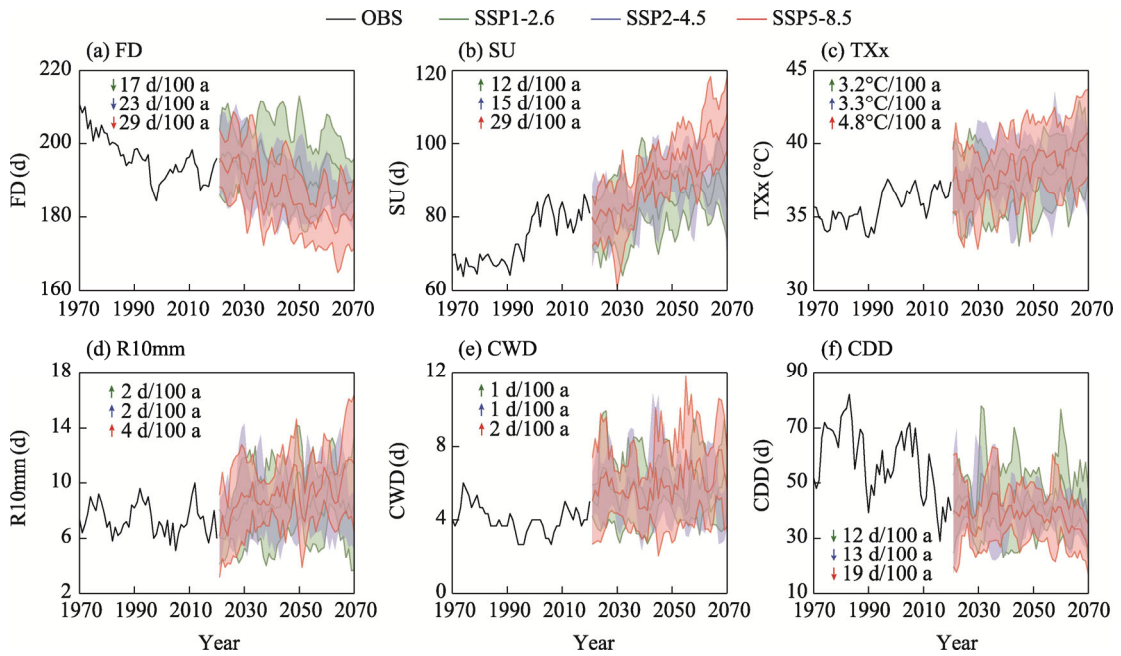


Fig. 3 Climate extremes in the model simulations of the Xilin River Basin from 1970 to 2020. (a), FD (frost days); (b), SU (summer days); (c), TXx (Max Tmax); (d), R10mm (heavy precipitation days); (e), CWD (consecutive wet days); (f), CDD (consecutive dry days). To enhance visual clarity, the figures show a three-year sliding average. The colored arrow indicates the average rate of change under each scenario. The shaded area indicates the range of the standard deviation of the REA results.

3.2.2 Climate extreme cycles

To determine the patterns of climate extremes, we applied a Morlet wavelet analysis to the climate extreme indices during the period of 1970–2020, yielding the Morlet wavelet analysis results shown in Figure 4. The energy distributions of the six climate extreme indices, as shown in Figure 4a–f, shared similar characteristics, predominantly displaying a "high–low–high" pattern within a cycle of 20–30 a. Notably, R10mm exhibited a more distinct and continuous cyclic oscillation over a cycle of 15 a, covering a significant portion of the time domain. The wavelet variance plots (Fig. 4g–l) further showed that these indices each manifested three prominent peaks. The primary peak periods (most dominant cycles) for FD, SU, TXx, R10mm, CDD, and CWD were 26, 27, 27, 27, 25, and 27 a during the period of 1970–2020, respectively, indicating that these indices had their most pronounced cyclical oscillations within the range of 25–27 a.

During the period of 1970–2020, the second most dominant cycles for these indices were 9, 42, 43, 7, 10, and 9 a, respectively, while the third most dominant cycles were 43, 8, 8, 46, 41, and 45 a, respectively.

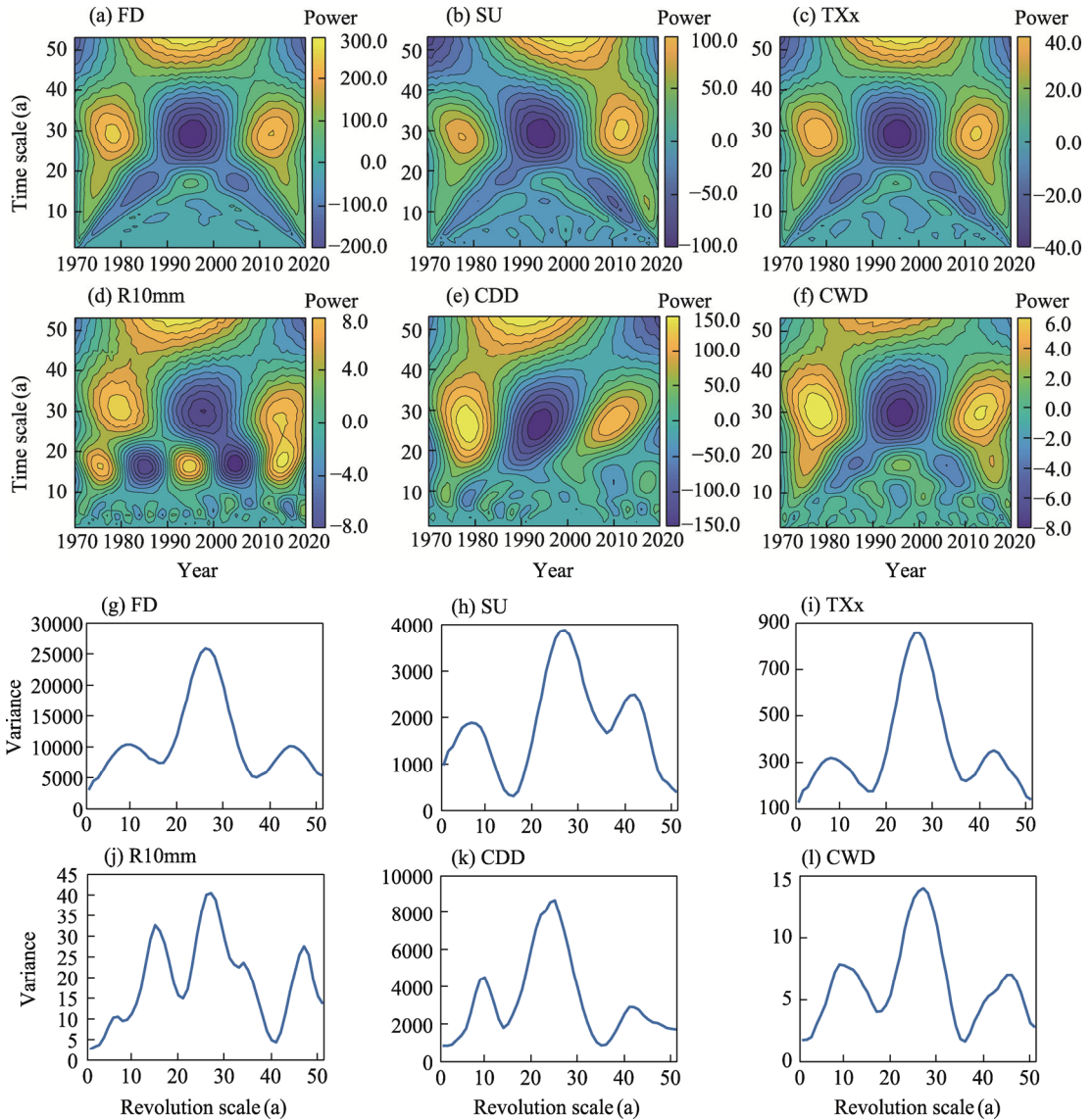


Fig. 4 Time-series characteristics of climate extreme changes based on a Morlet wavelet analysis: continuous wavelet power spectrum (a–f) and wavelet variance (g–l). (a and g), FD; (b and h), SU; (c and i), TXx; (d and j), R10mm; (e and k), CDD; (f and l), CWD.

3.3 Variations in the SPEI

Figure 5 shows the characteristics of the variations for the SPEI in the Xilin River Basin across different time periods. Following a linear fitting, the SPEI exhibited a slight decreasing trend under different climate scenarios, with trend rates of $-0.003/\text{a}$, $-0.003/\text{a}$, $-0.004/\text{a}$, and $-0.008/\text{a}$ during the historical period (1970–2020) and during the future period (2021–2070) under the SSP1-2.6, SSP2-4.5, and SSP5-8.5 scenarios, respectively. With the increase in the climate extremes under each scenario, the trend toward aridification became more severe. To further determine the SPEI trend, we performed a sliding t -test with a four-year scale on the SPEI to detect the mutation points. The critical value for significance was ± 2.45 at the 0.05 level.

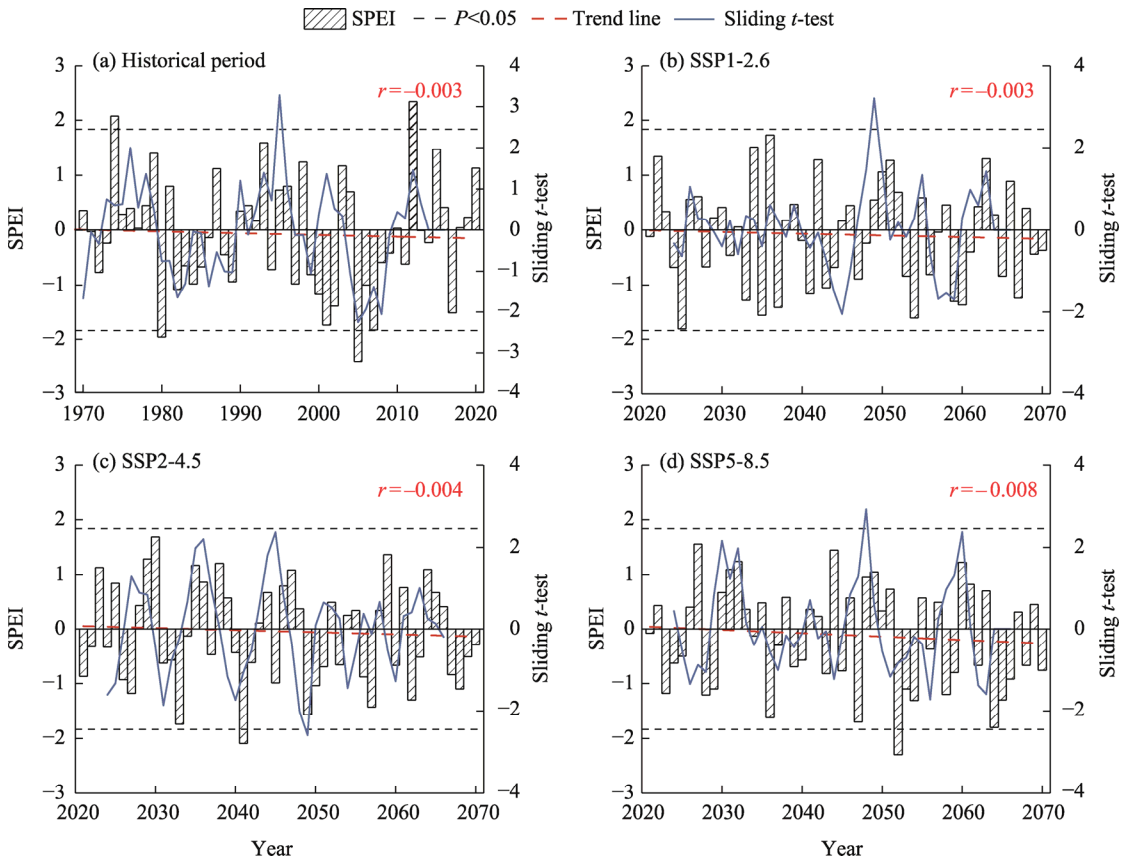


Fig. 5 Variations of the Standardized Precipitation Evapotranspiration Index (SPEI) and sliding t -test results during the historical period from 1970 to 2020 (a) and during the future period from 2021 to 2070 under different climate scenarios (b–d) in the Xilin River Basin

Based on the results of the sliding t -test, we identified abrupt changes of the SPEI in 1995 during the historical period (1970–2020), and in 2049 (under the SSP1-2.6 scenario), 2045 (under the SSP2-4.5 scenario), and 2048 (under the SSP5-8.5 scenario) during the future period (2021–2070), all of which passed the significance test at the 95% level. This indicated that the variability of annual meteorological drought conditions in the Xilin River Basin is significant.

Table 4 details the annual frequency of various drought classes in the Xilin River Basin, and provides information of the SPEI differences under the three climate scenarios. During the historical period, 17 drought events were recorded, while during the future period, 18, 19, and 22 drought events were expected to occur under the SSP1-2.6, SSP2-4.5, and SSP5-8.5 scenarios, respectively, indicating an anticipated increase in drought frequency. During the historical period and during the future period under the three climate scenarios (SSP1-2.6, SSP2-4.5, and SSP5-8.5), mild droughts occurred 9, 7, 10, and 11 times respectively, while moderate to severe droughts occurred 8, 11, 9, and 11 times, respectively.

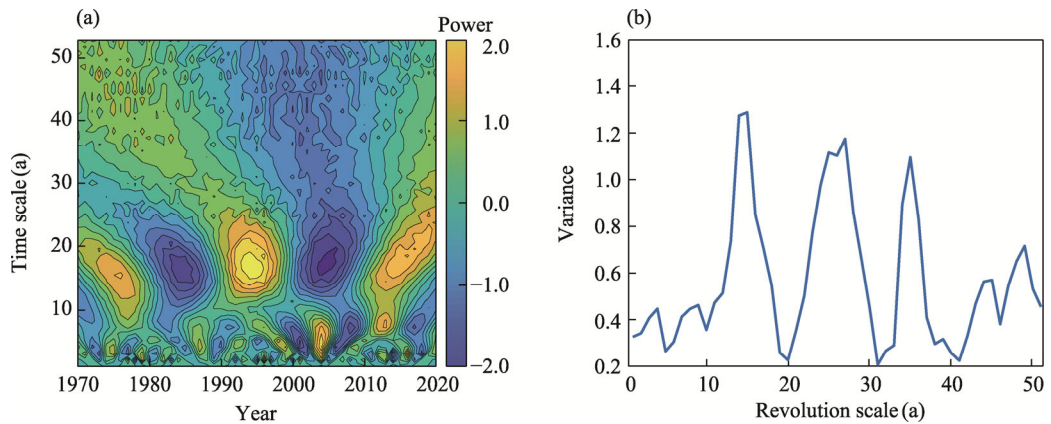
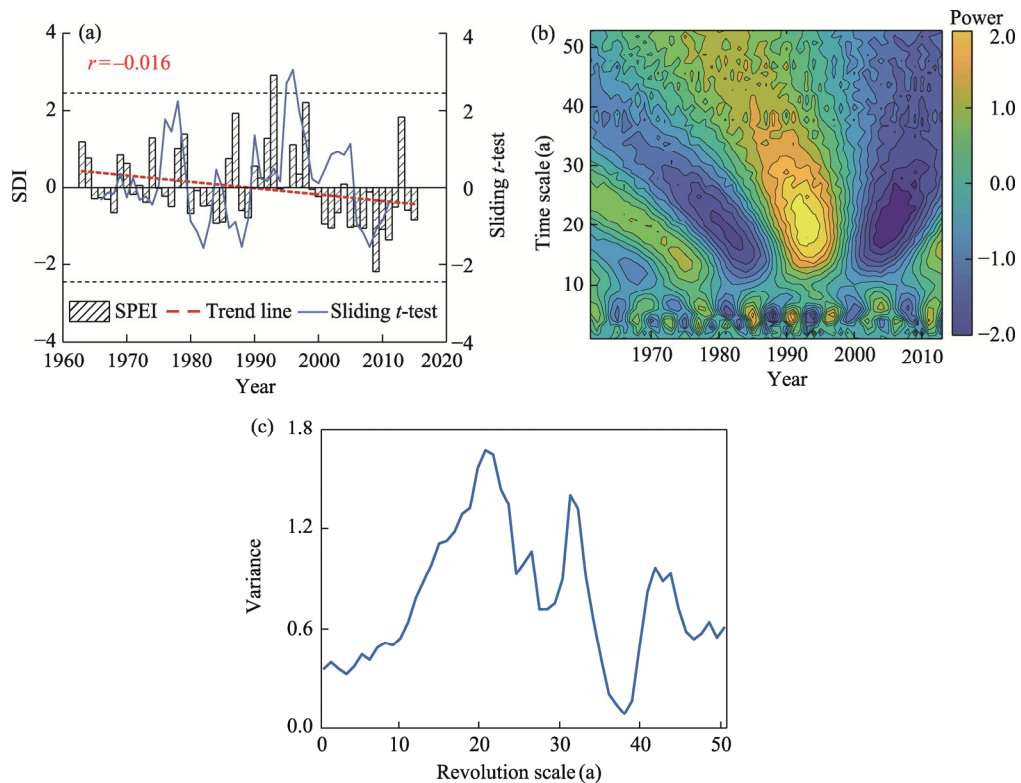
Because the SPEI is affected by various factors, its energy distribution exhibited different periodic oscillations at different time scales (Fig. 6a). From the analysis of Figure 6b, it is determined that the SPEI had three major periodic changes at 10–20, 20–31, and 31–41 a. The SPEI exhibited a pronounced alternating pattern of wet and dry oscillations at the first dominant period of 15 a.

3.4 Correlation analysis between drought and climate extremes

Figure 7 presents the SDI trend of runoff (Fig. 7a) and its periodic variations (Fig. 7b–c) in the Xilin River from 1963 to 2015. Figure 7a reveals alternating dry and wet periods in runoff,

Table 4 Frequency of meteorological drought in the Xilin River Basin during the historical period (1970–2020) and during the future period (2021–2070) under the three climate scenarios (SSP1-2.6, SSP2-4.5, and SSP5-8.5)

Drought level	Frequency of meteorological drought (times)			
	Historical period	SSP1-2.6	SSP2-4.5	SSP5-8.5
Mild drought	9	7	10	11
Moderate drought	3	7	6	7
Severe drought	4	4	2	3
Extreme drought	1	0	1	1
Total	17	18	19	22

**Fig. 6** Change characteristics of the SPEI time-series based on a Morlet wavelet analysis. (a), continuous wavelet power spectrum; (b), wavelet variance.**Fig. 7** Change characteristics of the Streamflow Drought Index (SDI) time-series from 1963 to 2015 based on a Morlet wavelet analysis. (a), trend analysis; (b), continuous wavelet power spectrum; (c), wavelet variance. The sidebar in Figure 7b indicates correlation values ranging from -2.0 to 2.0 .

with a general trend toward increased aridity, decreasing at a rate of 0.016/a as determined by a linear fitting. A sliding t -test revealed a significant change in runoff in 1996, with a prolonged drought from 1999 to 2012. Figure 7b shows that, similarly to the SPEI, the oscillation energy density of the SDI varied across different time scales, characterized by multiple short-period oscillations. The Morlet wavelet analysis identified the primary, secondary, and tertiary dominant periods of the SDI as 22, 32, and 43 a, respectively (Fig. 7c).

Figure 8 is the correlation heatmap showing the relationships among the climate extreme indices, SPEI, and SDI. A particularly strong positive correlation was observed between the SPEI and SDI. The SDI and SU exhibited a negative correlation of -0.41 ($P<0.01$), while the SDI and R10mm exhibited a positive correlation of 0.33 ($P<0.05$). However, the correlations between the SDI and other indices were relatively weak. The SPEI had strong correlations with SU, CWD, and R10mm, with correlation coefficients of -0.32 ($P<0.05$), 0.28 ($P<0.05$), and 0.51 ($P<0.01$), respectively.

To further explore these relationships and their effects on the SDI, we employed the wavelet coherence analysis approach, which is a time-frequency resonance method. The results are shown in Figure 9. Among the climate extreme indices, FD had no significant influence on the dominant properties of the SDI, suggesting a minor impact on the long-term changes of the SDI. This indicates that these indices fluctuated more rapidly than the SDI over a cycle of 2–7 a. Both R10mm and SDI had a significant positive correlation with a notable 1-a resonant period during 1985–1990.

There were four significant resonance periods between the SPEI and SDI (Fig. 9g). At the 2–3 a periodic scale during the period of 1980–2000, the arrows pointed to the upper right, indicating that the SPEI was a quarter cycle ahead of the SDI. However, during the period of 1990–2000, the SPEI displayed a clear lag at the 8–12 a scale. Additionally, at the 4–6 a scale, the energy and continuity of the conjugate periods of the SPEI and SDI were stronger and exhibited a continuous and significantly positive correlation, with the conjugate periods spanning the entire time series within the cone of influence.

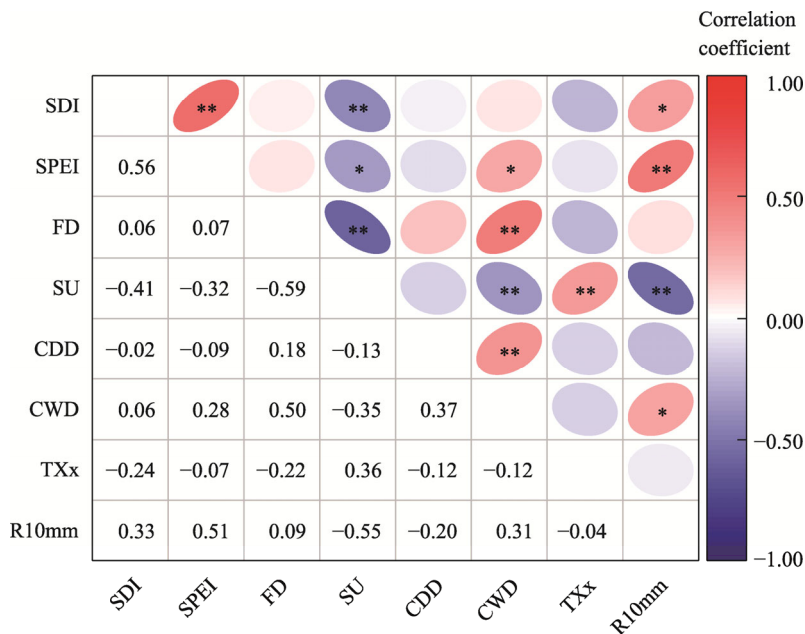


Fig. 8 Correlation heatmap showing the relationships among the climate extreme indices, SPEI, and SDI. *, $P<0.05$ level; **, $P<0.01$ level. Ellipses pointing toward the upper right indicate positive correlations, while those pointing toward the upper left indicate negative correlations. The flatter the ellipse and the darker its color, the stronger the correlation.

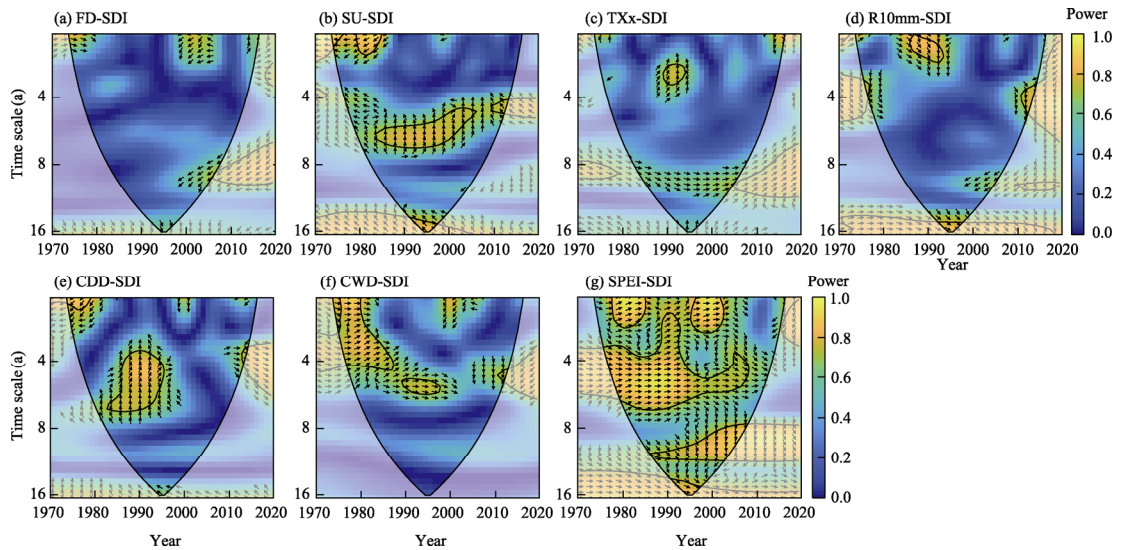


Fig. 9 A wavelet coherence analysis showing the relationships of climate extreme indices and the SPEI with the SDI during the period of 1970–2020. (a), relationship between FD and SDI; (b), relationship between SU and SDI; (c), relationship between TXx and SDI; (d), relationship between R10mm and SDI; (e), relationship between CDD and SDI; (f), relationship between CWD and SDI; (g), relationship between the SPEI and SDI. The color bar indicates the covariance strength (power), with yellow representing strong co-movements and blue indicating weak ones. The black contoured shaded area marks the 5% significance level, and the black thick circles within the cone of influence highlight segments where the correlation between the series is statistically significant at the 95% confidence level. Additionally, the phase relationship is denoted by the arrow directions, with the upward and downward arrows indicating that climate extreme indices lead and lag the SDI, respectively. The left and right arrows suggest the anti-phase and in-phase relationships between the series, respectively.

4 Discussion

Climatic and hydrological variations are complicated in arid areas. Although the accuracy of forecast data has greatly improved through downscaling and multi-model ensemble methods, precipitation data still contain larger errors than temperature data, which is related to the difficulty in simulating precipitation characteristics in GCMs (Stephens and Ellis, 2008).

The results of the analysis of climate extreme indices revealed likely increases in extreme high temperatures, decrease in extreme cold temperatures, and an intensification of precipitation extremes in the future in the Xinlin River Basin. This was consistent with previous CMIP5-based studies in this basin (Han et al., 2018; Zhu et al., 2021). The magnitude of index changes and variability was usually larger for the higher forcing scenarios (SSP5-8.5>SSP2-4.5>SSP1-2.6), with the uncertainty increasing over time. This suggests that temperature and precipitation may be particularly sensitive to CO₂ emissions, highlighting the importance of considering climate change when formulating social development policies (Li et al., 2013).

All temperature-based extreme indices (FD, SU, and TXx) showed a warming trend in the Xinlin River Basin in the future, which may lead to increased wildfires, landslides, heatwaves, and crop damage, adversely affecting human health and ecosystems (Rehana et al., 2024). This warming trend will directly result in more frequent and intense heatwaves, exacerbating the negative impacts of drought and high temperatures on agricultural production and food security (Hassan et al., 2024). Additionally, heatwaves may increase the incidence of heatstroke, cardiovascular diseases, and respiratory problems, while also worsening air quality and further impacting public health (Ascaso et al., 2024; Zhao et al., 2024). In this study, R10mm index displayed an increasing trend under all future scenarios, which implies the occurrence of more heavy precipitation events in the future. Combined with the decrease in CDD and increase in CWD, the drought conditions in the Xilin River Basin may be slightly alleviated in the future, but

the effect could be minimal.

The SPEI exhibited a trend toward drought during the period of 1970–2020. Both the frequency and trend of drought occurrence, and the drought conditions in the Xilin River Basin were expected to intensify under all future scenarios. Li et al. (2021) indicated that under the SSP1-2.6, SSP2-4.5, and SSP5-8.5 scenarios, 65%, 89%, and 99% of the arid areas in Asia, respectively, will experience more persistent and intense droughts. Further analysis revealed that there was an abrupt change point of drought in the Xilin River Basin in 1995 (Fig. 5), after which the drought intensity increased markedly. Zhang et al. (2020a) confirmed that the SPEI of the Xilin River Basin experienced an inflection point toward drought starting from the 1990s. Under the future climate scenarios, we simulated a similar mutation point to occur in the Xilin River Basin in the 2040s.

During the historical period (1970–2020) in the Xilin River Basin, the primary cycle of the climate extreme indices was 24–27 a, while the main cycles for the SPEI and SDI were 17 and 22 a, respectively. The abrupt change year for the SDI was 1996 in this study, which was 5 a earlier than the abrupt change year for the runoff depth in the Xilin River as identified by Zhang et al. (2019a). This discrepancy may be due to the different time scales and indices selected in the studies. In the Xilin River Basin, there was a highly significant positive correlation between the SPEI and SDI, a significant positive correlation between R10mm and SDI, and a highly significant negative correlation between SU and SDI. This indicates that runoff in the Xilin River is sensitive to heavy precipitation events, temperature changes, and variations of potential evapotranspiration. Wang et al. (2024a) found that precipitation is usually the main factor affecting river runoff variations in arid areas. However, this study revealed that in the Xilin River Basin, the SDI was more sensitive to SU than to R10mm. This is because in semi-arid areas, the lower soil moisture content and vegetation cover limit the impact of heavy precipitation events on the SDI because surface runoff and rapid evaporation occur without the rapid replenishment of groundwater (Owuor et al., 2016). During the period of 1980–2000 in the Xilin River Basin, the SPEI was more responsive on short-term scales than the SDI, but it lagged on long-term scales after 1990. This is likely due to the immediate impacts of short-term climatic events such as the El Niño–Southern Oscillation (Shukla et al., 2024). Conversely, the SDI was ahead of the SPEI in the latter stages and was influenced by changes in local land uses and water management systems. After the 1990s, increased grazing and urbanization resulted in more fragmented landscapes and a reduced wetland area in the Xilin River Basin (Zhou et al., 2020; Lv et al., 2024). Under the higher forcing scenarios in the future, the frequency of extreme weather events and hydrological droughts is expected to significantly increase, potentially leading to more severe environmental problems. Addressing this issue through reduced greenhouse gas emissions and sustainable development policies is crucial for mitigating future climate impacts.

5 Conclusions

This study analyzed and predicted the characteristics of variations in climate extreme indices and droughts in the Xilin River Basin during the historical period from 1970 to 2020 and during the future period from 2021 to 2070 and explored the relationships between them. After bias correction, the accuracy of climate data was enhanced using climate models. Predictions using a multi-model ensemble were more reliable than those from single models, with reduced errors and improved correlations, particularly for temperature forecasts. Under the higher forcing scenarios (e.g., SSP2-4.5 and SSP5-8.5), both extreme high temperatures and heavy precipitation events became more frequent and intense, while extreme cold temperatures became less common. The Xilin River Basin is expected to warm and experience more intense precipitation in the future under all climate scenarios. The climate is expected to become drier in the future. Additionally, the climate extreme indices exhibited significant periodic fluctuations, with R10mm having a cycle of 15-a and other climate extremes displaying cycles of 24–27 a. Furthermore, there were significant correlations among the SPEI, SDI, SU, and R10mm. Overall, the SDI exhibited greater

lag effects at lower frequency scales, while the climate extreme indices tended to precede the onset of drought.

These findings enable a more comprehensive understanding of climatic and hydrological processes in arid and semi-arid areas under climate change and have the potential to reduce the uncertainties in predictions of climate extremes and droughts. Due to limitations in the available data, we were unable to predict the SDI of runoff. However, we anticipate future runoff trends to lean toward increased aridification. We recommend that more comprehensive data are collected to construct hydrological models that will assist in effective drought management in arid and semi-arid areas in the future.

Conflict of interest

The authors declare that they have no competing financial interests or personal relationships that may have influenced the work reported in this paper.

Acknowledgements

This work was funded by the Central Guidance on Local Science and Technology Development Fund of Inner Mongolia Autonomous Region, China (2022ZY0153) and the "One Region Two Bases" Supercomputing Capacity Building Project of Inner Mongolia University, China (21300–231510).

Author contributions

Writing - original draft preparation, formal analysis, visualization, software, methodology, and conceptualization: QU Zhicheng; Investigation, software, and validation: YAO Shunyu; Writing - review and editing, supervision, funding acquisition, and resources: LIU Dongwei. All authors approved the manuscript.

Open Access This article is licensed under a Creative Commons Attribution 4.0 International License, which permits use, sharing, adaptation, distribution and reproduction in any medium or format, as long as you give appropriate credit to the original author(s) and the source, provide a link to the Creative Commons licence, and indicate if changes were made. The images or other third party material in this article are included in the article's Creative Commons licence, unless indicated otherwise in a credit line to the material. If material is not included in the article's Creative Commons licence and your intended use is not permitted by statutory regulation or exceeds the permitted use, you will need to obtain permission directly from the copyright holder. To view a copy of this licence, visit <http://creativecommons.org/licenses/by/4.0/>.

References

- Almazroui M. 2019. Climate extremes over the Arabian Peninsula using RegCM4 for present conditions forced by several CMIP5 models. *Atmosphere*, 10(11): 675, doi: 10.3390/atmos10110675.
- Ascaso M S, Diaz J, Lopez-Bueno J A, et al. 2024. How heatwaves affect short-term emergency hospital admissions due to bacterial foodborne diseases. *Science of the Total Environment*, 946: 174209, doi: 10.1016/j.scitotenv.2024.174209.
- Ballarin A S, Barros G L, Cabrera M C, et al. 2021. A copula-based drought assessment framework considering global simulation models. *Journal of Hydrology: Regional Studies*, 38: 100970, doi: 10.1016/j.ejrh.2021.100970.
- Bilgili F, Kocak E, Kuskaya S, et al. 2022. Co-movements and causalities between ethanol production and corn prices in the USA: New evidence from wavelet transform analysis. *Energy*, 259: 124874, doi: 10.1016/j.energy.2022.124874.
- Chikabvumbwa S R, Salehnia N, Gholami A, et al. 2024. Characterization of hydro-meteorological droughts based on dynamic future scenarios and effective rainfall over Central Malawi. *Theoretical and Applied Climatology*, 155(3): 1959–1975.
- Dong J A, Xing L Q, Cui N B, et al. 2023. Standardized precipitation evapotranspiration index (SPEI) estimated using variant long short-term memory network at four climatic zones of China. *Computers and Electronics in Agriculture*, 213: 108253, doi: 10.1016/j.compag.2023.108253.
- Fattah M A, Hasan M M, Dola I A, et al. 2024. Implications of rainfall variability on groundwater recharge and sustainable management in South Asian capitals: An in-depth analysis using Mann Kendall tests, continuous wavelet coherence, and innovative trend analysis. *Groundwater for Sustainable Development*, 24: 101060, doi: 10.1016/j.gsd.2023.101060.
- Gao S R, Jiang G L, Zhang Z Q, et al. 2024. Permafrost temperature dynamics and its climate relations in various Tibetan alpine

- grasslands. *Catena*, 241: 108065, doi: 10.1016/j.catena.2024.108065.
- Gao X, Shi Y, Song R, et al. 2008. Reduction of future monsoon precipitation over China: Comparison between a high resolution RCM simulation and the driving GCM. *Meteorology and Atmospheric Physics*, 100(4): 73–86.
- Gumus V. 2023. Evaluating the effect of the SPI and SPEI methods on drought monitoring over Turkey. *Journal of Hydrology*, 626: 130386, doi: 10.1016/j.jhydrol.2023.130386.
- Han T T, Chen H P, Hao X, et al. 2018. Projected changes in temperature and precipitation extremes over the Silk Road Economic Belt regions by the Coupled Model Intercomparison Project Phase 5 multi-model ensembles. *International Journal of Climatology*, 38(11): 4077–4091.
- Harrison S P, Bartlein P J, Izumi K, et al. 2015. Evaluation of CMIP5 palaeo-simulations to improve climate projections. *Nature Climate Change*, 5(8): 735–743.
- Hassan W U, Nayak M A, Azam M F. 2024. Intensifying spatially compound heatwaves: Global implications to crop production and human population. *Science of the Total Environment*, 932: 172914, doi: 10.1016/j.scitotenv.2024.172914.
- Kuskaya S. 2022. Residential solar energy consumption and greenhouse gas nexus: Evidence from Morlet wavelet transforms. *Renewable Energy*, 192: 793–804.
- Laimighofer J, Laaha G. 2022. How standard are standardized drought indices? Uncertainty components for the SPI & SPEI case. *Journal of Hydrology*, 613: 128385, doi: 10.1016/j.jhydrol.2022.128385.
- Li H W, Li Z, Chen Y N, et al. 2021. Projected meteorological drought over Asian drylands under different CMIP6 scenarios. *Remote Sensing*, 13(21): 4409, doi: 10.3390/rs13214409.
- Li J F, Zhang Q, Chen Y Q, et al. 2013. Changing spatiotemporal patterns of precipitation extremes in China during 2071–2100 based on earth system models. *Journal of Geophysical Research: Atmospheres*, 118(22): 12537–12555.
- Li J Z, Li Y P, Zhang T, et al. 2023. Research on the future climate change and runoff response in the mountainous area of Yongding watershed. *Journal of Hydrology*, 625: 130108, doi: 10.1016/j.jhydrol.2023.130108.
- Liu Y, Li Y P, Huang G H, et al. 2023. Development of an integrated model on the basis of GCMs-RF-FA for predicting wind energy resources under climate change impact: A case study of Jing-Jin-Ji region in China. *Renewable Energy*, 219: 119547, doi: 10.1016/j.renene.2023.119547.
- Lv X Q, Liu J H, Balzter H K, et al. 2024. Rapid and extensive expansion of shrub encroachment into grassland in Xilin Gol League, China, and its driving forces. *International Journal of Applied Earth Observation and Geoinformation*, 132: 104009, doi: 10.1016/j.jag.2024.104009.
- Medeiros F J, Oliveira C P, Avila-Diaz A. 2022. Evaluation of extreme precipitation climate indices and their projected changes for Brazil: From CMIP3 to CMIP6. *Weather and Climate Extremes*, 38: 100511, doi: 10.1016/j.wace.2022.100511.
- Mohammed S, Arshad S, Alsilibe F, et al. 2024. Utilizing machine learning and CMIP6 projections for short-term agricultural drought monitoring in central Europe (1900–2100). *Journal of Hydrology*, 633: 130968, doi: 10.1016/j.jhydrol.2024.130968.
- Nayak P C, Venkatesh B, Krishna B, et al. 2013. Rainfall-runoff modeling using conceptual, data driven, and wavelet based computing approach. *Journal of Hydrology*, 493: 57–67.
- Nourani V, Tootoonchi R, Andaryani S. 2021. Investigation of climate, land cover and lake level pattern changes and interactions using remotely sensed data and wavelet analysis. *Ecological Informatics*, 64: 101330, doi: 10.1016/j.ecoinf.2021.101330.
- Omer A, Elagib N A, Ma Z G, et al. 2020. Water scarcity in the Yellow River Basin under future climate change and human activities. *Science of the Total Environment*, 749: 141446, doi: 10.1016/j.scitotenv.2020.141446.
- Owuor S O, Butterbach-Bahl K, Guzha A C, et al. 2016. Groundwater recharge rates and surface runoff response to land use and land cover changes in semi-arid environments. *Ecological Processes*, 5(1): 16, doi: 10.1186/s13717-016-0060-6.
- Rehana S, Nannaka V, Mummidivarapu S K. 2024. Variations of compound warm, dry, wet, and cold climate extremes in India during 1951 to 2014. *Science of the Total Environment*, 950: 175164, doi: 10.1016/j.scitotenv.2024.175164.
- Ren L W, Zhou T J, Zhang W X. 2020. Attribution of the record-breaking heat event over Northeast Asia in summer 2018: the role of circulation. *Environmental Research Letters*, 15(5): 054018, doi: 10.1088/1748-9326/ab8032.
- Rezvani R, Rahimimovaghar M, Na W, et al. 2023. Accelerated lagged compound floods and droughts in northwest North America under 1.5°C–4°C global warming levels. *Journal of Hydrology*, 624: 129906, doi: 10.1016/j.jhydrol.2023.129906.
- Samuel S, Dosio A, Mphale K, et al. 2023. Comparison of multi-model ensembles of global and regional climate model projections for daily characteristics of precipitation over four major river basins in southern Africa. Part II: Future changes under 1.5°C, 2.0°C and 3.0°C warming levels. *Atmospheric Research*, 293: 106921, doi: 10.1016/j.atmosres.2023.106921.
- Sang Y F. 2013. A review on the applications of wavelet transform in hydrology time series analysis. *Atmospheric Research*, 122: 8–15.
- Savage A, Bambrick H, Gallegos D. 2021. Climate extremes constrain agency and long-term health: A qualitative case study in

- a Pacific Small Island Developing State. *Weather and Climate Extremes*, 31: 100293, doi: 10.1016/j.wace.2020.100293.
- Shukla S, Zaheer F, Hoell A, et al. 2024. ENSO-based outlook of droughts and agricultural outcomes in Afghanistan. *Weather and Climate Extremes*, 45: 100697, doi: 10.1016/j.wace.2024.100697.
- Stephens G L, Ellis T D. 2008. Controls of global-mean precipitation increases in global warming GCM experiments. *Journal of Climate*, 21(23): 6141–6155.
- Su B D, Huang J L, Mondal S K, et al. 2021. Insight from CMIP6 SSP-RCP scenarios for future drought characteristics in China. *Atmospheric Research*, 250: 105375, doi: 10.1016/j.atmosres.2020.105375.
- Su Y J, Zhang P D, Su Y Q. 2015. An overview of biofuels policies and industrialization in the major biofuel producing countries. *Renewable and Sustainable Energy Reviews*, 50: 991–1003.
- Sun Q H, Miao C Y, Duan Q Y. 2016. Extreme climate events and agricultural climate indices in China: CMIP5 model evaluation and projections. *International Journal of Climatology*, 36(1): 43–61.
- Thornthwaite C W. 1948. An approach toward a rational classification of climate. *Geographical Review*, 38(1): 55–94.
- Tripathi I M, Mahto S S, Kushwaha A P, et al. 2024. Dominance of soil moisture over aridity in explaining vegetation greenness across global drylands. *Science of the Total Environment*, 917: 170482, doi: 10.1016/j.scitotenv.2024.170482.
- Villarini G, Vecchi G A. 2012. Twenty-first-century projections of North Atlantic tropical storms from CMIP5 models. *Nature Climate Change*, 2(8): 604–607.
- Wang Q Z, Sun Y F, Guan Q Y, et al. 2024a. Exploring future trends of precipitation and runoff in arid regions under different scenarios based on a bias-corrected CMIP6 model. *Journal of Hydrology*, 630: 130666, doi: 10.1016/j.jhydrol.2024.130666.
- Wang S P, Zhang Q, Liu Y Z, et al. 2024b. Effects of global warming on drought onset in China. *Journal of Hydrology*, 632: 130964, doi: 10.1016/j.jhydrol.2024.130964.
- Yu K, Hui P H, Zhou W D, et al. 2021. Evaluation of extreme temperature in multi-RCM simulations over CORDEX-East Asia phase II domain. *Atmospheric Research*, 255: 105535, doi: 10.1016/j.atmosres.2021.105535.
- Zhang A L, Gao R Z, Liu T X, et al. 2019a. Identification on hydrometeorology mutation characteristics and ecological evolution pattern of the plateau inland river basin-taken Xilin River and Balager River of Inner Mongolia for instance. *China Environmental Science*, 39(12): 5254–5263. (in Chinese)
- Zhang L, Zhu Z Y, Xi X K, et al. 2020a. Analysis of drought evolution in the Xilin River basin based on standardized precipitation evapotranspiration index. *Arid Zone Research*, 37(4): 819–829. (in Chinese)
- Zhang L, Zhu Z Y, Wang H M, et al. 2020b. Analysis of hydrological drought evolution characteristics and influencing factors in Xilin River basin. *Journal of Soil and Water Conservation*, 34(4): 178–184, 192. (in Chinese)
- Zhang L X, Chen X L, Xin X G. 2019b. Short commentary on CMIP6 Scenario Model Intercomparison Project (ScenarioMIP). *Advances in Climate Change Research*, 15(5): 519–525. (in Chinese)
- Zhao C, Brissette F, Chen J. 2023. Projection of future extreme meteorological droughts using two large multi-member climate model ensembles. *Journal of Hydrology*, 618: 129155, doi: 10.1016/j.jhydrol.2023.129155.
- Zhao C, Huang Y S, Cheng Y B, et al. 2024. Association between heatwaves and risk and economic burden of injury related hospitalizations in China. *Environmental Research*, 259: 119509, doi: 10.1016/j.envres.2024.119509.
- Zhao J C, Zhang J J, Hu Y W, et al. 2022. Effects of land uses and rainfall regimes on surface runoff and sediment yield in a nested watershed of the Loess Plateau, China. *Journal of Hydrology: Regional Studies*, 44: 101277, doi: 10.1016/j.ejrh.2022.101277.
- Zhou Y J, Liu T X, Duan L M, et al. 2020. Driving force analysis and landscape pattern evolution in the upstream valley of Xilin River Basin. *Arid Zone Research*, 37(3): 580–590. (in Chinese)
- Zhou Y J, Batelaan O, Guan H D, et al. 2024. Assessing long-term trends in vegetation cover change in the Xilin River Basin: Potential for monitoring grassland degradation and restoration. *Journal of Environmental Management*, 349: 119579, doi: 10.1016/j.jenvman.2023.119579.
- Zhu H H, Jiang Z H, Li L. 2021. Projection of climate extremes in China, an incremental exercise from CMIP5 to CMIP6. *Science Bulletin*, 66(24): 2528–2537.